J. Phys. Soc. Jpn.
Downloaded from journals.jps.jp by 161.111.10.232 on 07/21/21

Journal of the Physical Society of Japan **87**, 061005 (2018)
https://doi.org/10.7566/JPSJ.87.061005

Photoelectron Diffraction and Holography Studies of 2D Materials and Interfaces

Mikhail V. Kuznetsov[1], Ilya I. Ogorodnikov[1], Dmitry Yu. Usachov[2], Clemens Laubschat[3], Denis V. Vyalikh[2,4,5], Fumihiko Matsui[6], and Lada V. Yashina[7*]

[1]*Institute of Solid State Chemistry of the Ural Branch of the Russian Academy of Sciences, Pervomayskaya Str. 91, 620990 Ekaterinburg, Russia*
[2]*St. Petersburg State University, 7/9 Universitetskaya nab., St. Petersburg, 199034, Russia*
[3]*Institute of Solid State Physics, Dresden University of Technology, D-01062 Dresden, Germany*
[4]*Departamento de Fisica de Materiales and CFM-MPC UPV/EHU, Donostia International Physics Center (DIPC), 20080 San Sebastian, Spain*
[5]*IKERBASQUE, Basque Foundation for Science, 48011 Bilbao, Spain*
[6]*Nara Institute of Science and Technology, Ikoma, Nara 630-0192, Japan*
[7]*M.V. Lomonosov Moscow State University, Leninskie Gory 1/3, 199991 Moscow, Russia*

(Received August 18, 2017; accepted October 24, 2017; published online April 3, 2018)

Photoelectron diffraction (XPD) and holography (XPH) are powerful spectroscopic methods that allow comprehensive exploration and characterization of certain structural properties of materials, in particular those of 2D systems and interfaces. Recent developments in XPD and XPH are especially impressive when they are applied to partially disordered systems such as intercalation compounds, doped graphene, buffer layers or adsorbates and imperfectly ordered germanene and phoshporene. In our brief review, we sum up the advances in XPD and XPH studies of 2D materials and discuss the unique opportunities granted by these two interrelated methods.

1. Introduction

Photoelectron diffraction (XPD)[1–10] is a powerful structural method of surface science that acts at the atomic scale. It combines the element identification features of low-energy ion scattering spectroscopy (LEIS) and X-ray photoemission spectroscopy (XPS) with the structural precision of low-energy electron diffraction (LEED) and surface X-ray diffraction (SXRD). At the same time, it is free of the disadvantages related to possible surface damage in LEIS and to the lack of possibility to identify the elemental composition and, hence, stronger model dependence of LEED. In photoelectron holography (XPH) the diffraction pattern is considered to be a hologram, which is converted into a real-space image of the atomic structure, thus enabling direct reconstruction of the local environment around the atom of interest. Here, no assumptions about the structure are required a priori. Previously, this relatively new method was successfully applied to visualize, with a moderate accuracy of ~0.5 Å, the atomic structure for simple cases of elemental solids, such as metals.[11,12] First successful applications of holography for compounds or alloys have also already been reported.[13–15]

An important feature of XPD and XPH is that the atoms of interest should occupy similar crystal lattice sites but not necessarily be ordered in the long range. To produce the diffraction pattern they only need to have the same orientation of their local environment. This opens up remarkable possibilities for studies of dopants and adsorbed atoms, which frequently appear randomly distributed over the lattice sites or in a surface layer. An additional benefit granted by XPD and XPH is that these methods are not only element-specific but also sensitive to individual charge state of the element, provided that the diffraction pattern is measured with sufficient energy resolution. Surface sensitivity can be varied by adjusting the kinetic energy of the emitted electrons, however, on the one hand, probing of the very surface layer by both XPD and XPH fails as compared to that by the scanning tunneling microscopy (STM) and LEIS. This issue is naturally overcome for true 2D materials like single layers of graphene or h-BN grown heteroepitaxially on a substrate. On the other hand, by adjusting the relevant structural model one can study subsurface layers up to tens of monolayers thick.

Many examples of XPD applications are summarized already in the reviews by Woodruff,[16–19] Fadley,[1,2,20–22] and other authors.[23–25] Much less reports are related to XPH.[11,26–28] For now, the renaissance of photoelectron diffraction is due to prominent advances in this field, namely, first, impressive development of experimental tools, especially electron energy analyzers that allow fast acquisition of full-hemisphere diffraction patterns, and application of new tools for data treatment and structure determination like, for instance, SPEA-MEM algorithm[29–32] in holography; second, advances of XPD for molecules probed with a free-electron laser;[33–35] third, the application of tender X-rays (2–10 keV)[20,36,37] in photoelectron diffraction that allow probing buried interfaces.

Nowadays, the development and broader applications of XPD and XPH are closely related to the unflagging interest to 2D materials and interfaces. The most well-studied 2D crystals are graphene and its relatives — phosphorene, silicene, germanene, stanene. Another class of compound materials is presented by few (3–7) layer 2D crystals cut from the bulk layered structures with strong covalent in-plane bonds and relatively weak stacking of these atomic layers by van der Waals forces. They feature MoS_2, WS_2 and other 3d metal chalcogenides, GaS, GaSe, GaTe, InSe, Bi_2Se_3, Bi_2Te_3, Sb_2Te_3 etc.

In our brief review, we sum up the current advances in XPD and XPH studies of 2D materials and discuss the unique opportunity granted by these methods, as well as certain restrictions related to each specific case.

2. X-ray Photoelectron Diffraction and Holography of Graphene and Related 2D Materials

2.1 Graphite and graphene

The first example of holographic reconstruction for a

©2018 The Author(s)
This article is published by the Physical Society of Japan under the terms of the Creative Commons Attribution 4.0 License. Any further distribution of this work must maintain attribution to the author(s) and the title of the article, journal citation, and DOI.

J. Phys. Soc. Jpn.
Downloaded from journals.jps.jp by 161.111.10.232 on 07/21/21

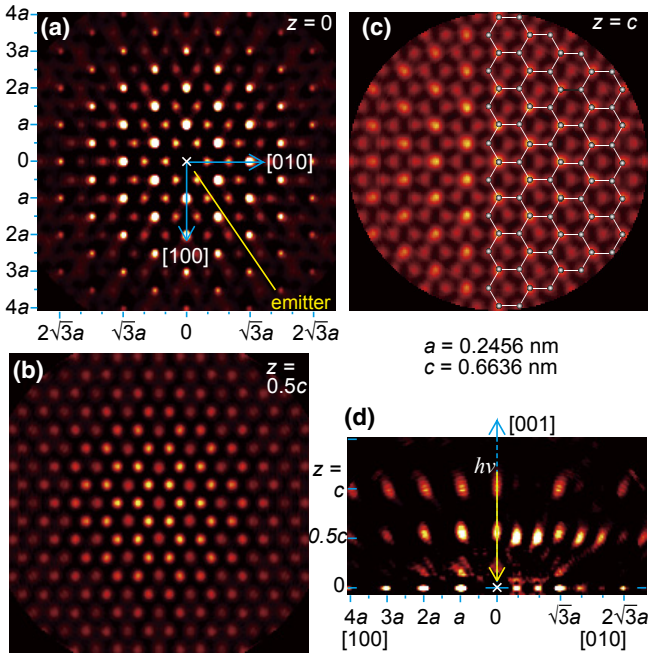

Fig. 1. (Color online) Cross sections of the real-space reconstructed images for grapthite surface. (a) The graphite layer including the emitter atom, (b) the first and (c) the second layers above the emitter atom, and (d) vertical cross sections of the real-space images for the *xz* (left) and *yz* (right) planes are shown.[38)]

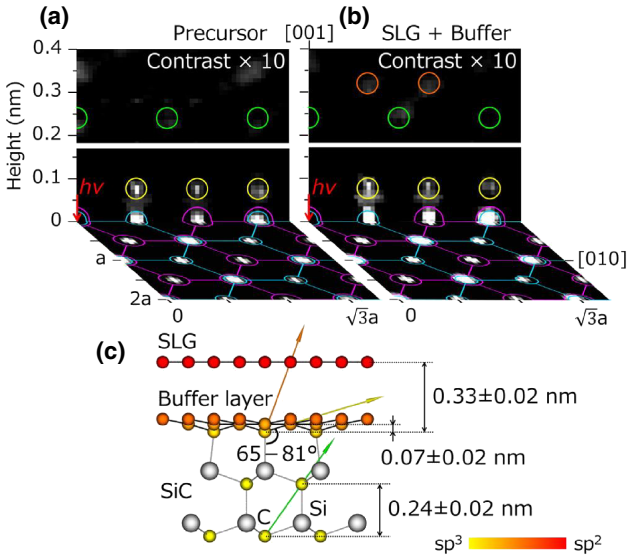

Fig. 2. (Color online) (a, b) The reconstructed real-space atomic images of the precursor layer and SLG as well as the buffer layer. The SLG region with the height of 0.2–0.4 nm was separately shown to enhance the signal contrast by the factor of 10. (c) Cross-sectional model of SLG on the SiC(0001). Reprinted with permission from Ref. 40. © 2015 Elsevier.

layered material structure based on the photoelectron diffraction data was demonstrated by Matsui et al. in their case study of graphite single crystal surface.[38)] They recorded a series of 2π diffraction patterns for graphite single crystal surface at different kinetic energies of C 1s photoelectrons in the range of 311–908 eV. Using the whole dataset and taking into account the fact that images from different sites are overlapping, the spatial images of the three surface layers of graphite were reconstructed with sufficiently high clearness as presented in Fig. 1 with the help of the reconstruction algorithm based on the fitting of elemental diffraction patterns for various C–C bond distances. The contribution of each layer to XPD pattern was thoroughly evaluated. Finally, the holographic method allowed detailed visualization of the in-plane structure of carbon layers as well as their relative arrangement. Interatomic distances in the carbon atomic layers were determined with the precision of 1%, while for the interlayer distance the accuracy was 3%.

In the recent publication of the same authors[39)] the photoelectron holography method was successfully applied to discover the atomic structure of the surface of a bimetal-intercalated graphite superconductor $(Ca,K)C_8$ obtained by cleavage. This layered material possesses the highest superconducting transition temperature of 11.5 K in this class of materials. It was established that the cleavage preferentially occurs along the layers intercalated by K atoms and containing no Ca atoms, which indicates weaker interlayer bonding in these parts of the crystal. The authors have directly obtained the images of carbon and potassium atomic arrangements in the surface layer of $Ca_{0.11(3)}K_{0.89(3)}C_{7.1(4)}$ crystal reconstructed from the C 1s and K 2p photoelectron holograms. It was found that the local structures differ substantially from those suggested by the bulk $(Ca,K)C_8$ crystal structure as determined by X-ray diffraction. In detail, the K atoms were found to be located in the centers of C hexagons of the graphene sheets stacked in the AA arrangement with an interlayer spacing of 5.7 Å. In addition, in the same crystal the non-intercalated graphite-layered structure was confirmed to exhibit AB stacking with an interlayer spacing of 3.3 Å. This work[39)] is an illustrative example of photoelectron holography as a unique method for 3D visualization of local atomic structures at the surface region; it also indicates its high potential for structural studies of graphene and other 2D materials.

Large-scale graphene, which is currently an established platform for future (nano)electronics, can be grown as a single or multiple layers either on metals, or on different carbides terminated with a buffer carbon layer, on h-BN and rarely on several other substrates. The properties of graphene-based electronics depend strongly on the structure of graphene-substrate interface and the corresponding interaction.

The photoelectron diffraction and holography methods were applied to study the surface structures that are formed during the synthesis of graphene on the 4H-SiC(0001) surface[40,41)] to gain deeper understanding of the structure of a buffer or precursor layer that is formed between the substrate and graphene. The structure of graphene on top of the buffer layer was visualized as it is shown in Fig. 2. The separation between the single-layer graphene (SLG) and the buffer layer was found to be 0.33 ± 0.02 nm, which is close to the interlayer spacing in graphite; the stacking sequence was identified as the one of the AB type.

A further step towards comprehensive understanding of graphene on 6H-SiC(0001) was taken by application of chemical state selective XPD.[42,43)] The authors studied epitaxial graphene layers grown on a 6H-SiC(0001) substrate by means of thermal decomposition. The fact is that different carbon atoms located in the graphene lattice, in the silicon carbide substrate, or in the buffer layer have resolvable chemical shifts in the C 1s core level photoemission spectra.

©2018 The Author(s)

J. Phys. Soc. Jpn.
Downloaded from journals.jps.jp by 161.111.10.232 on 07/21/21

In Ref. 42 for each chemical state full hemispherical XPD patterns were extracted and analyzed. One should mention that in these experiments the photon energy was carefully chosen, so that for the C 1s electron the kinetic energy (KE) was about 165 eV. At this energy the multiple scattering and backscattering regime dominates, so that each C 1s component has strong sensitivity to a particular chemical environment. Whereas for the Si 2p peak the authors used the energy of 348.5 eV, at which the forward scattering regime begins to dominate, so that the Si 2p emission was suitable to probe the stacking structure and the number of graphite layers. By comparing the experimental data with the model XPD patterns calculated within the multiple scattering theory the authors concluded that while graphene is strictly flat, the buffer layer shows a more complex structure with a long-range rippling and buckling at the atomic scale. The displacement of the sublattices is more intense when the buffer layer is not covered with graphene. This ripple-buckling model structure agrees with a sp^2 to sp^3 rehybridization (pyramidalization) that affects the stability of this layer and explains the difference in certain electronic properties between graphene and the buffer layer. Similar results were obtained in Ref. 43, where the authors analyzed azimuthal and polar diffraction curves with chemical state resolution as well.

In the work of Parreiras et al.[44] the structure of the single-layer graphene/Ni(111) interface was studied by LEED and photoelectron diffraction in the angular-mapping mode. The authors synthesized graphene on the Ni(111) surface several times and obtained non-identical dependencies of the intensity of electron diffraction maxima on electron energy (I–V curves), which indicated different relative positions of the carbon and nickel atoms. LEED simulations demonstrated that among the twelve studied samples the data obtained from five of them were in good agreement with the so-called top-fcc structure, where the atoms of one carbon sublattice are located above the metal surface atoms, while the second sublattice is adsorbed above the atoms of the third nickel layer (fcc sites). Three data sets indicated the bridge-top structure, where the centers of the C–C bonds are located above the topmost Ni atoms. The rest of samples were described as a mixture of top-fcc and bridge-top structures. This is in accordance with the STM data, which reveal coexistence of different structures, and with the DFT calculations, which predict a very small energy difference between them.[45] The XPD data were obtained for only one of the samples and they agreed well with the top-fcc model.

The authors of the present review used the chemical splitting of the XPS C 1s peak of graphene for the structural analysis of both pristine graphene/Co(0001) system and the one doped with boron impurities that substitute the carbon atoms.[46] The XPD measurements were performed in the varying energy mode at a fixed emission angle. In the case of well-oriented undoped graphene/Co(0001) the high-resolution C 1s XPS spectra exhibited two states corresponding to the two carbon sublattices.

After doping with boron, a new carbon state related to carbon atoms with boron in its surroundings emerged in the C 1s spectrum (Fig. 3). XPD was utilized to identify the location of boron atoms and chemically non-equivalent carbon atoms. For this purpose the XPS C 1s spectra were

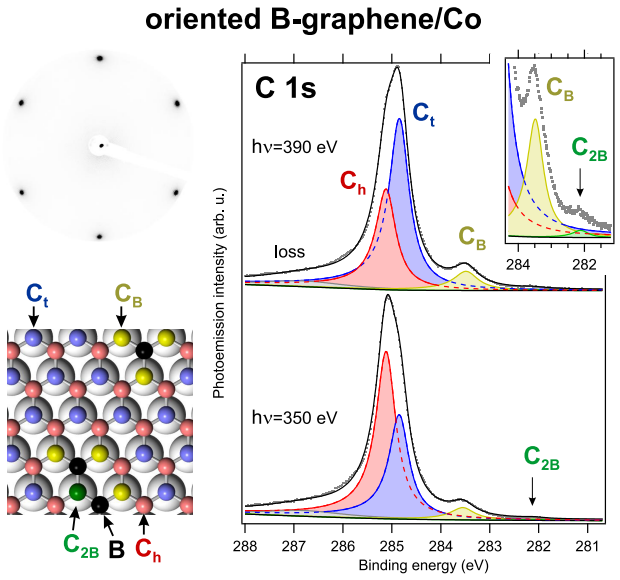

Fig. 3. (Color online) XPS spectra of the B-graphene/Co(0001) system with 2.4 at. % of boron impurities, obtained at two photon energies. The spectra exhibit three main maxima: the two peaks originate from the two non-equivalent carbon sublattices, located above the cobalt atoms (C_t) and above the hollow sites (C_h), while the third peak C_B corresponds to the carbon atoms having one neighbor boron atom. Due to PED effects, the intensities of these peaks change when the photon energy is varied. The presented hexagonal LEED pattern confirms the high quality of the graphene layer. Also the model of the B-graphene/Co interface is shown. Reprinted with permission from Ref. 46. © 2016 American Chemical Society.

acquired in the photon energy range of 305–560 eV with a step of 5 eV [Fig. 4(a)] and the corresponding diffraction curves were plotted for each component of the C 1s spectra, as shown at the bottom of Fig. 4(b). Theoretical calculations of the XPS curves for several structural models of the interface were performed using EDAC codes.[47]

Analysis of the photoelectron diffraction effects provided conclusive evidence for the sublattice asymmetry in pristine and boron-doped graphene grown on the Co(0001) substrate. In a well-oriented graphene/Co(0001) system one sublattice of carbon atoms is located above the Co atoms, while the other one occupies the hollow sites. This important property makes such interface an ideal platform for synthesis of doped graphene with impurities incorporated in only one of the two carbon sublattices. Such possibility is illustrated by the example of the B-graphene/Co(0001) system, where the boron impurities preferably substitute carbon atoms of one sublattice located above hollow sites of the substrate [see the lower panel of Fig. 4(c)].

The theory predicts that such asymmetric doping of graphene should induce a band gap, and the gap width can be controlled by the dopant concentration. The authors claim that B-graphene with the doping asymmetry is a novel material, which is worth considering as a good candidate for applications in graphene-based field-effect transistors (GFETs) or other electronic devices.

The possibility of efficient resolution of chemically non-equivalent carbon states in the C 1s photoemission spectra was used by Bingardi et al.[48] in the study of oxygen intercalation under graphene on a Ni(111) surface. In this work the authors used XPD with chemical state resolution,

©2018 The Author(s)

J. Phys. Soc. Jpn.
Downloaded from journals.jps.jp by 161.111.10.232 on 07/21/21

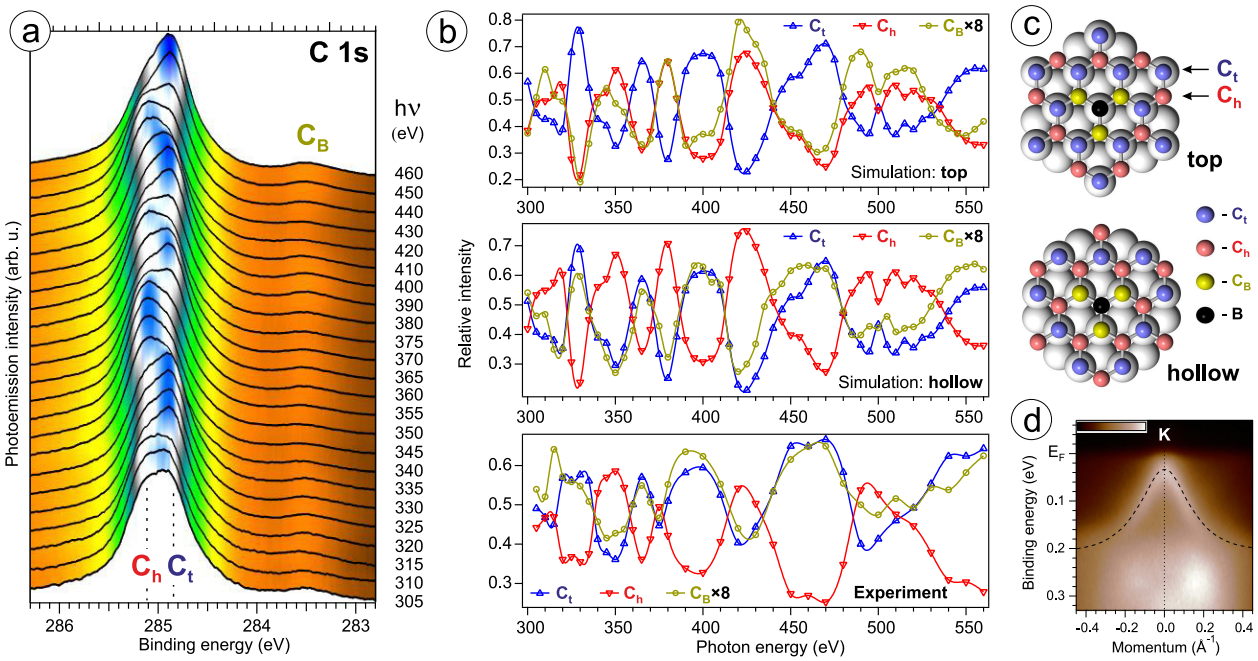

Fig. 4. (Color online) (a) C 1s XPS spectra of B-graphene/Co(0001) at a boron concentration of 2.4 at. % as a function of photon energy. (b) Measured relative intensities of the three components of the C 1s spectra C_t, C_h, and C_B (bottom graph), and theoretical curves calculated for the two structural models, shown in the panel (c), where the boron atoms occupy either top sites (top graph) or hollow sites (middle graph). Obviously, the hollow position of the boron atoms provides good agreement between the calculation and the experiment. (d) An ARPES image, measured with He I radiation ($h\nu = 21.2$ eV). Reprinted with permission from Ref. 46. © 2016 American Chemical Society.

however, in contrast to the above-discussed example, the angular XPD maps were measured. Comparison of the experimental data with the calculated XPD patterns led to a conclusion that graphene is adsorbed on the intercalated oxide without any well-defined configuration. It was revealed that domains aligned with the substrate and rotated domains were efficiently intercalated with oxygen. However, the rotated domains are pivotal to the intercalation process, being the first to be intercalated by chemisorbed oxygen. The aligned graphene domains are the first to be landed back on the clean metal during the deintercalation process, while oxygen remains chemisorbed under the rotated domains even at temperatures up to 680 K.[48)]

2.2 *Germanene*

Special mention should be made of the results of XPD studies of graphene-like 2D crystals such as germanene, phosphorene, silicene, stanene, and others. They exist in the form of a single layer, but some of them do not have any bulk counterparts. Unfortunately we could not find any XPD studies of silicene and stanene.

A germanene layer with a honeycomb structure was studied by XPD on the Al(111) surface by Derivaz et al.;[49)] XPD dependencies of the Al 2p and Ge 2p intensities were analyzed as a function of the polar angle for two azimuthal directions, namely $[\bar{1}10]$ and $[\bar{1}2\bar{1}]$. The Al 2p dependence exhibited sharp diffraction maxima related to the close-packed atomic rows in the Al lattice. On the contrary, in the angular dependencies of the Ge 2p XPS peak the diffraction effects were practically absent. The intensity variation is only 3–5%. The authors concluded that Ge atoms do not penetrate through the Al(111) surface. They are localized at the surface in the form of a two-dimensional (3×3) Ge layer, known as germanene. Its structure differs from the Ge single layer, which forms a bulk germanium crystal.[49)]

2.3 *Phosphorene*

Phosphorene is a very interesting object for XPD studies, as it is a 2D allotrope of phosphorus with honeycomb structure. It can be considered as a single layer of black phosphorus (BP).[50)] In contrast to graphene, where the carbon layer is basically planar, phosphorene has a very puckered structure, therefore, each phosphorene layer can be seen as a bilayer of P atoms [Figs. 5(a) and 5(b)]. Another important difference between phosphorene and graphene is the presence of a direct band gap in the first one, which is theoretically expected to vary with the number of phosphorene layers from ∼0.3 eV for bulk BP to ∼2 eV for a single layer.[50)] Since the band gap depends on the structure, it is important to establish the structural parameters of a phosphorene monolayer, which may differ notably from the bulk of BP.

In Ref. 50 the P 2p XPD patterns of bulk BP were measured with the use of synchrotron radiation at a photon energy of 350 eV, which corresponds to the photoelectron kinetic energy of ∼220 eV. Theoretical calculations of XPD images were performed with the MSCD package[9)] using the atomic cluster consisting of 245 atoms. Up to 8 photoelectron scattering events were taken into account. The structural parameters of the topmost phosphorene layer were determined by fitting the theoretical XPD data to the experimental ones on the basis of R-factor. Figures 5(e)–5(g) shows the maps of the R-factor as a function of the main structural parameters. The minimal value of the R-factor is located within the darkest area; it corresponds to the optimal lattice parameters.

©2018 The Author(s)

J. Phys. Soc. Jpn.
Downloaded from journals.jps.jp by 161.111.10.232 on 07/21/21

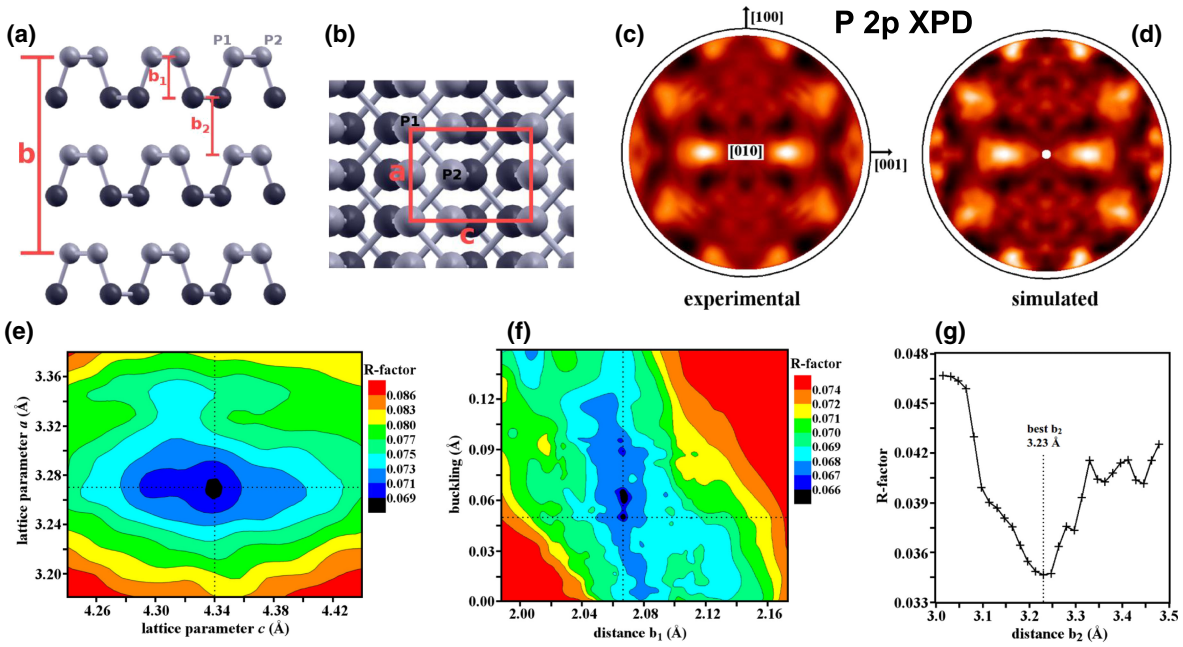

Fig. 5. (Color online) (a, b) Schematic illustration of the BP atomic structure. Side view (a) (*bc* plane) shows three bilayers (or three phosphorene layers). The P atoms are shown in different shades of grey for clarity. Top view (b) (*ac* plane) shows two bilayers and the in-plane unit cell. (c, d) Experimental and simulated photoelectron diffraction patterns. The patterns are orthographic projections. (e) Heat maps of the R-factor as a function of the lattice parameters *a* and *c*, (f) the b_1 distance and the buckling, and (g) the b_2 distance. Reprinted with permission from Ref. 50. © 2016 American Physical Society.

The authors of Ref. 50 concluded that the structure of the topmost phosphorene layer in black phosphorus is very similar to that expected for the bulk BP, probably due to the weak interaction between the phosphorene layers. The results also demonstrate that the topmost phosphorene layer is slightly displaced compared to the bulk structure and includes small contraction in the direction perpendicular to the surface. Additionally, some buckling is observed among the surface atoms. The contraction of the surface layer together with the buckling leads to uniformity in the length of the in-plane and inter-planar sp^3 bonds between the P atoms at the surface.

2.4 h-BN monolayer on d-metals

Single-layer thin films of hexagonal boron nitride (h-BN) on the surfaces of transition metals attract a lot of attention as an example of a metal–insulator interface. Moreover, the h-BN surface is considered as the best substrate for graphene layers with high mobility of charge carriers. Thus, it is not surprising that such an interesting material was systematically studied by photoelectron diffraction. We should note the works of Osterwalder et al. based on structural studies of the h-BN monolayer on the Ni(111) surface with XPD and STM.[23,51,52] It was shown that nitrogen atoms are located above nickel atoms, while boron atoms may occupy either fcc or hcp positions in different h-BN domains. As a result, a h-BN film consists of two types of domains rotated by 180° relative to each other. This result differs from the earlier work of the same authors, where they succeeded in producing a high-quality h-BN layer on the Ni(111) surface with one preferable type of adsorption geometry, namely fcc.[53] This is indicated by the B 1s XPD pattern that indicates a three-fold symmetry. The height difference between the B and N positions on the Ni(111) surface was estimated as 0.07 ± 0.06 Å.

The explanation of discrepancies in conclusions of the above-mentioned works can be found in the work of Orlando et al.[54] Here, the epitaxial h-BN monolayer was grown using a similar CVD approach, but on the surface of a different d-metal, namely on Ir(111). XPD with angular resolution was used as an analytic instrument for structure determination. It was shown that one-domain h-BN can be produced by a cyclic deposition of borazine on the Ir(111) surface at room temperature, followed by annealing at $T = 1270$ K. In this case a three-fold symmetry is observed in the N 1s and B 1s diffraction patterns. In contrast to this, a traditional high-temperature deposition of borazine ($T = 1070$ K) results in a h-BN layer formed by domains with opposite orientations. For such h-BN layers a six-fold symmetry of XPD patterns is typically observed. The authors recommend to pay attention to subtle nuances of h-BN deposition on transition metals and to use XPD for structural analysis.

An example of a successful application of XPD to investigation of a single h-BN layer on binary alloys is presented in Ref. 55. It was established that the top atomic layer of the PtRh(111) alloy is enriched in Rh, while the second layer is depleted of Rh, when a single layer of h-BN is grown on top. Using the angle-resolved XPS and XPD the authors have quantitatively estimated the surface enrichment with rhodium. Stereographic projections of the photoemission intensity of the Rh $3d_{5/2}$ and Pt $4f_{7/2}$ lines were measured before and after the h-BN synthesis [Figs. 6(a)–6(d)]. From these data the depth profiles of Pt concentration were extracted for each of the PtRh(111) and h-BN/PtRh(111) systems [Fig. 6(e)]. The results indicate that 80% of the top layer of bare PtRh consists of Pt atoms compared to 69% of Pt atoms in the second layer. After the h-BN growth the fit indicates 69% of Pt in the top layer and 81% of Pt in the second layer, which confirms the swapping of Pt and Rh in the first two layers and quantifies the amount

©2018 The Author(s)

J. Phys. Soc. Jpn.
Downloaded from journals.jps.jp by 161.111.10.232 on 07/21/21

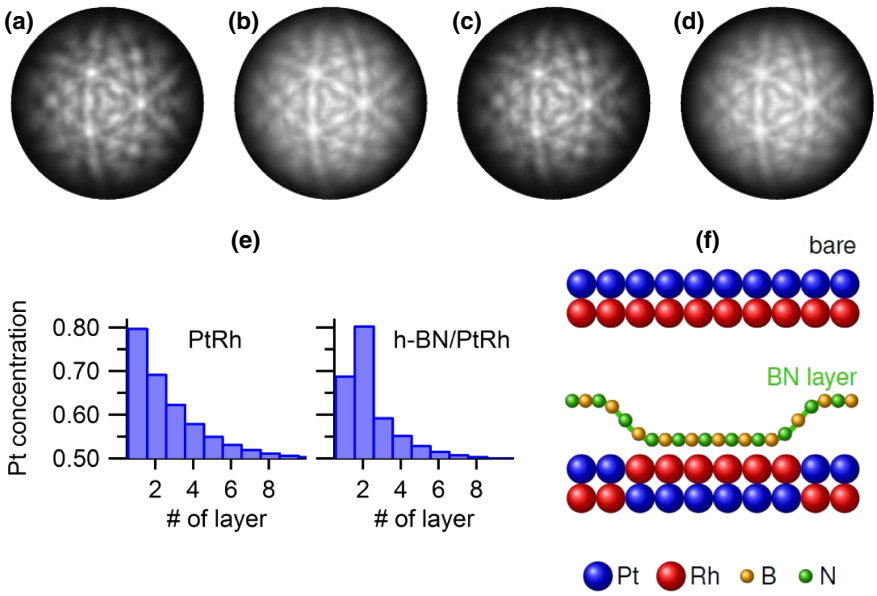

Fig. 6. (Color online) Mg K_α excited XPD patterns for Rh $3d_{5/2}$ (E_{kin} = 939.8 eV) and Pt $4f_{7/2}$ (E_{kin} = 1175.5 eV) emission. (a) Rh bare, (b) Pt bare, (c) Rh h-BN, and (d) Pt h-BN. (e) Pt concentrations as a function of the layer number. Note the swap of about 10% between the first and second layers. (f) The panel summarizes the lateral segregation scenario where the first two PtRh layers in the unit cell are represented by chains of 10 atoms. Reprinted with permission from Ref. 55. © 2016 American Physical Society.

to about 10 swaps per (10 × 10) unit cell. The fit results in a slightly larger (1.8 and 2.3 layers) decay constant of the excess Pt for the bare surface, which indicates that h-BN influences the segregation profile beneath the second layer. As a result, a model of the h-BN/PtRh(111) interface was proposed [Figs. 6(e) and 6(f)].[55)]

An interesting example of h-BN employment as a substrate for graphene is described in the work of Silvan Roth et al.,[56)] where a graphene/h-BN/Cu(111) heterostack was studied by means of LEED, STM, angle-resolved photoemission (ARPES), and XPD. The authors point out the two main problems of graphene use in electronics. First, it is difficult to grow large defect-free graphene crystals; second, an efficient approach for graphene synthesis on insulating substrates is required. A possible solution is synthesis of a graphene/h-BN/metal interface. In Ref. 56 the authors describe successful CVD synthesis of such interface and, among other interesting results, characterized it with photoelectron diffraction. Figure 7 shows the experimental B 1s, N 1s, and C 1s XPD data, as well as the corresponding theoretical diffraction patterns calculated within the multiple scattering formalism.

The B 1s and N 1s diffraction patterns of the hexagonal boron nitride in a graphene/h-BN/Cu(111) stack are characterized by the presence of strong maxima of forward scattering on the nearest in-plane neighbor atoms. These XPD data look quite similar to the h-BN XPD pattern without graphene.[53)] The C 1s XPD pattern also fits well the calculated diffraction of isolated graphene. From these data the authors draw a conclusion that the graphene layer is well-oriented and of a high quality. The absence of reflexes of forward scattering on carbon atoms in the B 1s and N 1s XPD results can be explained by an incommensurate structure of the graphene/h-BN interface.

Among the most recent works we should note a comprehensive study of the h-BN/Ni(111) interface by

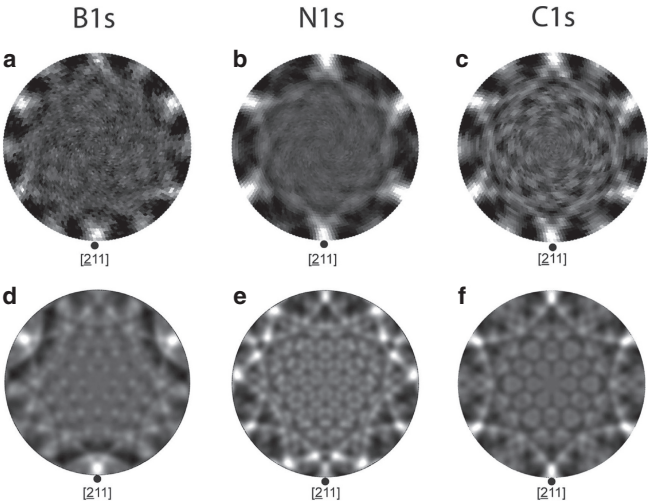

Fig. 7. Stereographic representation of experimental (top row) and theoretical (bottom row) photoelectron diffraction patterns of the B 1s, N 1s, and C 1s core levels displayed in a linear gray scale for polar emission angles between 0 and 82°. The experimental data are taken from a graphene/h-BN/Cu(111) stack, while the calculations were performed with a free-standing h-BN layer and a free-standing graphene layer, respectively, containing 120 atoms each. Reprinted with permission from Ref. 56. © 2013 American Chemical Society.

means of XPD with angular resolution in the energy-scanned mode.[57)] As already mentioned, the h-BN layer forms a commensurate (1 × 1) structure with nitrogen atoms adsorbed in the top positions and boron atoms preferably located in the fcc hollow sites, as shown in Figs. 8(a) and 8(b). Such non-equivalence of the B and N positions results in a slight buckling of the surface.

An experimental N 1s XPD pattern obtained for the h-BN/Ni(111) system is shown in Fig. 8. It demonstrates a six-fold symmetry, which is an indication of h-BN domains rotated by 180° with respect to each other. This case was already

©2018 The Author(s)

J. Phys. Soc. Jpn.
Downloaded from journals.jps.jp by 161.111.10.232 on 07/21/21

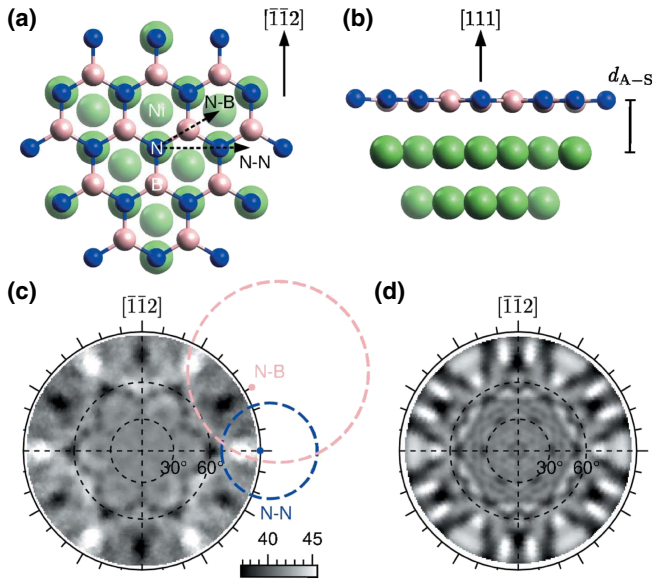

Fig. 8. (Color online) N 1s XPD of the h-BN/Ni(111) system at E_{kin} = 399 eV: (a, b) an atomic cluster used in the calculation, (a) top view and (b) side view; (c) experimental N 1s XPD diffraction cones (marked by circles) from scattering along the N–N and N–B nearest-neighbor directions corresponding to the dashed arrows in panel (a); (d) an N 1s XPD pattern calculated for the best-fit structural model of the h-BN/Ni(111) interface. Reprinted with permission from Ref. 57. © 2017 John Wiley & Sons.

discussed earlier in Refs. 23, 51, and 52. The authors suppose that in addition to the most stable top-fcc configuration a top-hcp structure with a slightly lower binding energy is also formed. A theoretical N 1s XPD pattern was calculated for the most probable structure using the EDAC code [Fig. 8(d)]. The calculation was performed with optimization of seven structural and non-structural parameters, including the distance between h-BN and the substrate, the corrugation of h-BN, the relaxation of the topmost Ni layer, the cluster size, the position of the refractive surface above the top layer, and the amplitude of the modulation function. As a result, the distance between the substrate and h-BN was found with energy-scanned XPD to be 2.11 ± 0.02 Å, which differs from the previously reported values obtained from LEED (2.222 Å[58]) and angle-scanned XPD (1.95 Å[52]).

3. X-ray Photoelectron Diffraction and Holography of Layered Chalcogenides

3.1 Transition metal dichalcogenides

Transition metal dichalcogenides typically possess distinct layered structure with three-atom-thick layers (X-M-X) stacked by weak van der Waals force [Fig. 9(e)]. Due to the quasi-2D structure these compounds exhibit a peculiar band structure and demonstrate a unique set of physical properties. One of the earliest XPD studies relates to a clean surface of MoS_2(0002) and adsorption structures that appear upon Cs deposition.[59] The surface structure was determined by comparing the polar and azimuthal diffraction curves with the simulated ones within the single scattering approximation (SSC). Further, $TiSe_2$, $TaSe_2$, and TaS_2 surfaces obtained by crystal cleavage (or exfoliation) were investigated in more detail.[60] Modelling of different possible configurations and their comparison with the experimental diffraction patterns

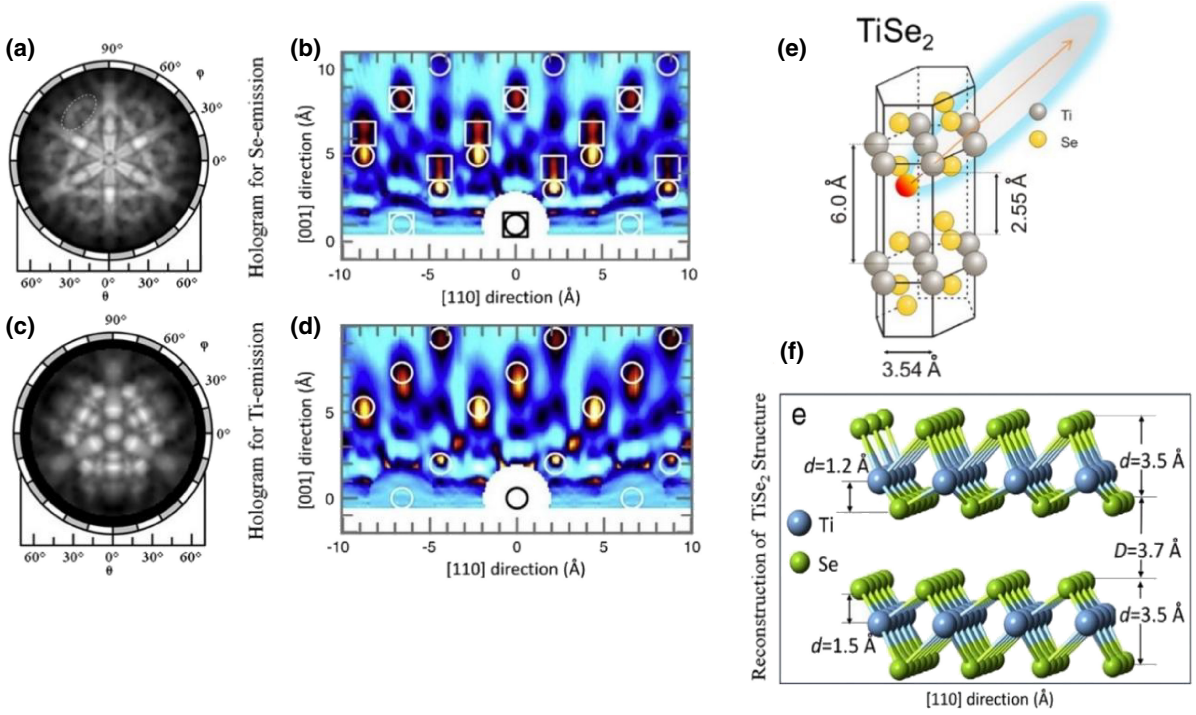

Fig. 9. (Color online) Reconstructed real space image of the 1*T*-$TiSe_2$ surface layer structure based on the Auger electrons Se(LMM) hologram (a) and a photoelectron hologram Ti 2p (c). For the Se(LMM) emission, the reconstructed pattern (b) is a superposition of two images, each of which corresponds to a fragment of the 1*T*-$TiSe_2$ structure surrounding two inequivalent positions of selenium atoms; circles denote the nearest neighbor atoms around the SeII-atom in the lower layer of the Se–Ti-SeII slab; while squares denote the Se nearest neighbor atoms in the upper layer of the Se–Ti-SeII slab. For the Ti 2p emission (d) circles denote the nearest neighbor atoms around a Ti atom. Positions are denoted according to those in an ideal crystal structure 1*T*-$TiSe_2$. (e) The unit cell of a layered crystal 1*T*-$TiSe_2$, (f) a model of the 1*T*-$TiSe_2$ surface derived from the two 3D-reconstructions of the Auger electrons Se(LMM) hologram and the photoelectron hologram Ti 2p. Reprinted with permission from Ref. 62. © 2012 Elsevier.

©2018 The Author(s)

J. Phys. Soc. Jpn.
Downloaded from journals.jps.jp by 161.111.10.232 on 07/21/21

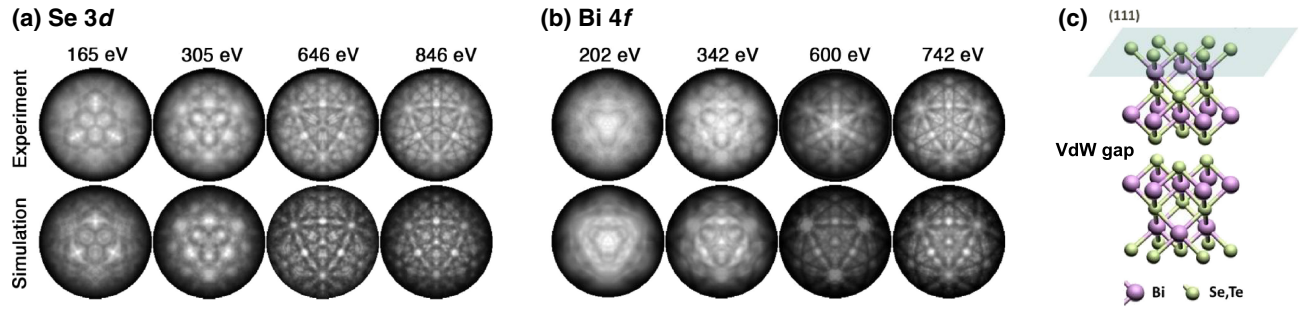

Fig. 10. (Color online) Experimental and EDAC-simulated (for structure 1 with bulk parameters) XPD patterns obtained for the Bi_2Se_3(111) surface at different electron kinetic energies for the Se 3d (a) and Bi 4f (b) core levels. (c) An atomic model of the Bi_2X_3(111) (X = Se, Te) structure. Reprinted with permission from Ref. 65. © 2015 American Physical Society.

allowed the authors to make a trivial conclusion that cleavage occurs along the van der Waals gap. In this case the calculations were also performed within the SSC and showed reasonable correlation with the experiment. Nevertheless, Despont et al.,[61] who also studied the 1*T*-TaS_2 surface, expressed certain scepticism concerning the SSC approach. In detail, they concluded that modelling within the single scattering approximation does not provide a reliable answer concerning the atomic structure, whereas the MSC-calculations describe the experimental observations well and allow distinguishing different polytypes related to the layer stacking (1*T* or 2*H*). Besides, it was proven that the surface is S-terminated.

In our earlier work,[62] we studied a clean surface of 1*T*-$TiSe_2$ using both XPD and XPH. Experimentally we measured the 2π-projections for both Ti 2p (E_{kin} = 1030 eV) and Se $L_3M_{45}M_{45}$ (E_{kin} = 1310 eV) and further made the corresponding calculations in the MSC-SW approximation using the EDAC code. Moreover, we used the SPEA-MEM[29–32] algorithm to reconstruct the 3D image of the atomic structure. The results are summarised in Fig. 9. In detail, Se atoms have two non-equivalent positions, and a Se diffraction pattern is a superposition of two respective patterns.[63] To resolve this issue we also calculated theoretical holograms for Se $L_3M_{45}M_{45}$. Finally, a comprehensive description of the surface atomic structure was obtained. Although the accuracy of our holography analysis is not high — about 0.1 Å — we concluded that the surface structure is close to that of the bulk but with notable distortions. These distortions are not supported by the complementary DFT modelling of an ideal surface and can be attributed to surface defects.

3.2 *Bismuth chalcogenides*

Tetradymite Bi_2Se_3 and Bi_2Te_3 are among the first studied topological insulators (TIs). TIs are characterized by topological interface or surface states (TSSs) demonstrating a peculiar spin state where electron spins are locked perpendicular to their linear momenta. The majority of studies on TIs, including the first observation of the TSS,[64] are related to the interface between the surface and the vacuum, i.e., the simplest trivial insulator. Topological insulator properties are of bulk nature but revealed at the surface or the interface. Therefore, detailed knowledge of the atomic structure is required.

In Ref. 65 we studied clean surfaces of Bi_2Se_3(111) and Bi_2Te_3(111) obtained by cleaving the bulk crystals. For Bi_2Se_3 the XPD patterns of the Bi 4f and Se 3d core levels for different kinetic energies are shown in Fig. 10. The EDAC-simulated diffraction patterns obtained for the structural model of the surface cut from the bulk structure [Fig. 10(c)] are provided for comparison. Our simulations both for Bi_2Se_3 and for Bi_2Te_3 immediately gives a very good reproduction of the experimental data.

To visualise the surface termination directly, we used photoelectron holography. To reconstruct the atomic structure of TIs, we applied the scattering pattern extraction algorithm together with the maximum entropy method as described by Matsushita et al.[29–32] Figure 11 shows a typical example of the local structure for a Se atom in the Bi_2Se_3(111) surface layer using a hologram. The 3D real space image was calculated from the experimental diffraction pattern shown in Fig. 11(a). For detailed analysis a cut along the gray plane in Fig. 11(a) is shown in Fig. 11(c) as a gray scale intensity image together with two line scans along A–A and B–B. In these profiles we observe overlaying atomic positions (marked with pink and green circles) hindering straightforward interpretation. This complexity arises from different positions of the Se emitter atoms in the crystal lattice with respect to the surface. The result of their combination is illustrated in the simulation shown in Fig. 12. From row 1 to 4 we move the position of the emitter atom to a deeper atomic layer. The respective Se emitter atom is marked with a circle. We show the simulated diffraction pattern in the second column and finally in the third column we provide the real space holography image calculated from the diffraction pattern. The deeper in the bulk we place the emitter atom, the more complex becomes the resulting holography image. Simultaneously, the diffraction pattern looks more similar to the one observed in the actual experiment (shown in Fig. 10). All in all, the results[65] suggest that the bulk structure remains intact and that the surface is Se terminated after the cleavage. All results are in good agreement with the Se–Bi–Se–Bi–Se layer sequence. The same approach was applied for the Bi 4f holograms. Similar results were also obtained for the Bi_2Te_3(111) surface, i.e., Te termination. The data obtained from the R-factor analysis and within the XPH approach are in good agreement with the data obtained by LEED for both Bi_2Se_3 and Bi_2Te_3.[66,67]

©2018 The Author(s)

J. Phys. Soc. Jpn.
Downloaded from journals.jps.jp by 161.111.10.232 on 07/21/21

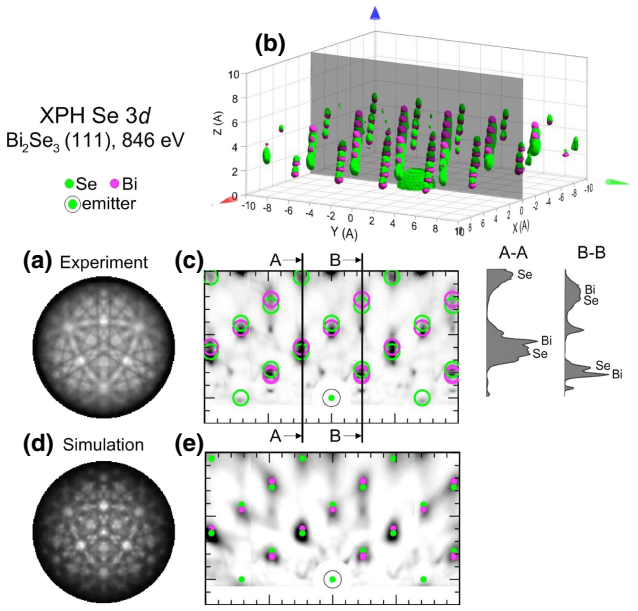

Fig. 11. (Color online) An example of the holographic reconstruction of a 3D-atomic structure for Se 3d obtained at a kinetic energy of 846 eV: an experimental XPD pattern (a); a real space image (b) and its cross section (c), a simulated XPD pattern (d), and a simulated real space image (e) obtained for the Se-terminated surface (structure 1). Reprinted with permission from Ref. 65. © 2015 American Physical Society.

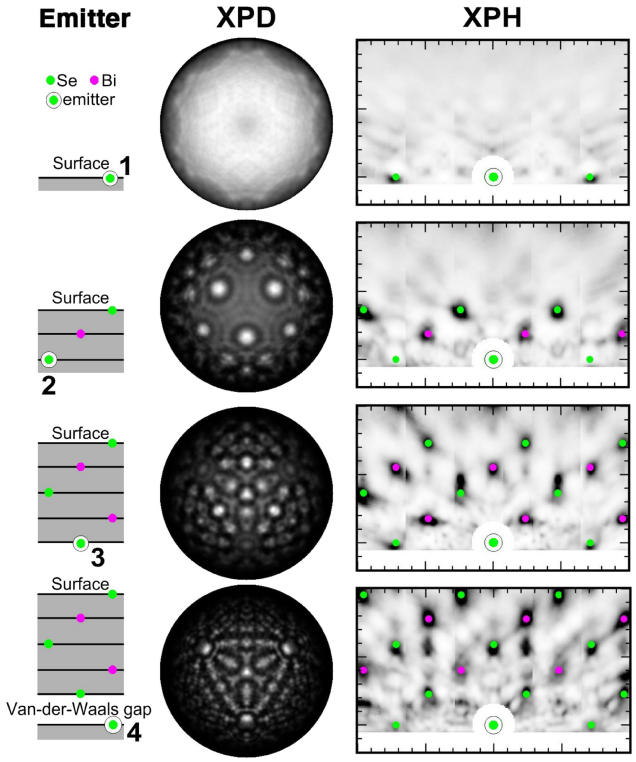

Fig. 12. (Color online) Contributions of different atomic positions of a Se emitter to the diffraction pattern and the real space image presented in Fig. 11(e): left column, the emitter position (marked as atoms in a ring); middle column, the calculated XPD pattern for a given emitter; right column, the calculated real space image for a given emitter. Reprinted with permission from Ref. 65. © 2015 American Physical Society.

Adsorption/intercalation structures on the surfaces of tetradymite TIs were studied for Ag[68] and Fe.[69] In Ref. 68 the diffraction patterns for clean and Ag-modified surfaces were compared; from this comparison the location of Ag atoms in the vdW gap was derived.

In Ref. 69 we studied structures formed after deposition of 1 and 2 ML of Fe on Bi_2Te_3(111) and observed a distinct Fe 3p diffraction pattern shown in Fig. 13(a). To reconstruct the Fe environment we used X-ray photoelectron holography. The results are illustrated in Fig. 13(b). One can see four atomic layers above the Fe emitter. From typical atomic distances it can be concluded that Te–Fe–Bi–Te–Fe–Bi–Te is the proper assignment of the in-depth atomic layers. Further we checked the stability of the most probable structure based on the DFT calculations. The calculated structure in Fig. 13(c) was found to be quite stable and we used the structural parameters as a starting point for the EDAC simulation, and they were further refined by R-factor analysis. We also exploited the unique capability of chemical state selective photoelectron diffraction to determine the atomic surrounding of a specific element in different charge states, i.e., showing different chemical shifts. Due to chemical interaction the Bi 4f spectra possess a complex structure as it is clearly seen in Fig. 13(f). We treated the Bi 4f spectra with two components for simplicity and derived two resulting diffraction patterns corresponding to the bulk and the surface components. For the surface component we applied the same structural model described above and found a perfect correlation.

An illustration of our approach to discover the atomic structure of the shallow interface is presented in Fig. 13(e). It includes the assessment of different sets of spectroscopic and diffraction data. Based on photoelectron holography of the impurity atom emitter the local environment was reconstructed in real space by XPH, then the structure was tested for stability by DFT, and further verification was provided using chemically state selective Bi 4f XPD as well as by comparing the calculated and the experimental core-level shifts. For the structure obtained this way, the interatomic distances were refined by R-factor analysis after the EDAC simulation of the diffraction patterns.

4. Conclusions and Outlook

Advances of XPD and XPH are especially impressive when these methods are applied to partially disordered systems such as intercalation compounds, doped graphene, buffer layers or adsorbates, and non-ideally ordered germanene and phoshporene. For instance, application of photoelectron holography to the graphite intercalation compound, $(K,Ca)C_8$, allows figuring out the local environment of the intercalate. K atoms were found to be located in the centers of the C hexagons of the graphene sheets stacked in the AA arrangement. For graphene grown on SiC, chemical-state-selective XPD and XPH allowed gaining deep understanding of the structural organization and the chemical nature of the buffer layer between flat graphene and the substrate. Chemical-state-resolved XPD allowed determination of preferred positions of boron impurities in graphene grown on a Co(0001) surface. It was demonstrated that XPD provides an efficient tool for controlling the asymmetry of graphene sublattices on the large scale. For layered semiconductors, mostly trivial results were obtained showing that the surface structure coincides with those cut from the bulk with

©2018 The Author(s)

J. Phys. Soc. Jpn.
Downloaded from journals.jps.jp by 161.111.10.232 on 07/21/21

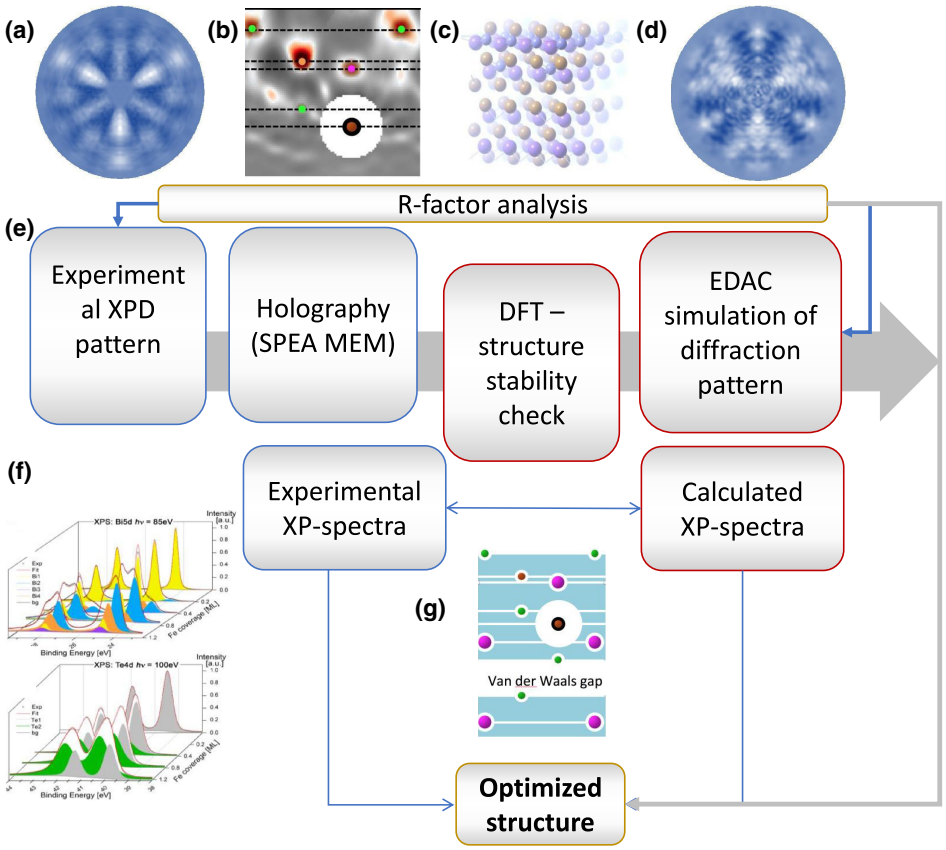

Fig. 13. (Color online) The scheme illustrates a paradigm to determine the local structure of foreign atoms at the interface using full hemisphere photoelectron diffraction data: (a) A Fe 3p experimental diffraction pattern for 2.2 ML Fe on Bi_2Te_3. (b) Holography reconstruction of the Fe local environment. (c) DFT simulated atomic model. (d) A simulated Fe 3p experimental diffraction pattern obtained for the optimized structure with 1/4 population of the position Fe 2. (e) Outline for the complex experimental and calculation procedure. (f) Example of XP-spectra for different coverages. (g) The resulting optimized structure.[69)]

chalcogen termination, as well as that there is negligible surface relaxation and no reconstruction, whereas for adsorbates we can directly use all advantages of the holography reconstruction of the local environment. This allows understanding the behavior of Ag on Bi_2Se_3(111) and Fe on Bi_2Te_3 and discovering specific structures responsible for their electronic and spin properties. All in all, XPD and XPH are powerful tools with their own range of applications, which provide in most cases rather unique information that is not available from other kinds of studies. In the future, one may anticipate rapid development of these techniques as they reach submicron lateral resolution that will allow overcoming the restrictions related to single-crystalline substrates.

Acknowledgments The authors acknowledge financial support of the Russian Foundation for Basic Research (Grant No. 16-29-06410). L.V.Ya. and D.Yu.U. acknowledge RSF (Grant No. 16-42-01093). C.L. acknowledges DFG (Grant Nos. LA655-17/1 and LA655-19/1). D.Yu.U. and D.V.V. acknowledge Saint Petersburg State University for research Grant No. 11.65.42.2017.

*yashina@inorg.chem.msu.ru

1) C. S. Fadley, Prog. Surf. Sci. **16**, 275 (1984).
2) C. S. Fadley, Surf. Sci. Rep. **19**, 231 (1993).
3) A. Kaduwela, D. Friedman, and C. Fadley, J. Electron Spectrosc. Relat. Phenom. **57**, 223 (1991).
4) J. J. Rehr and R. C. Albers, Phys. Rev. B **41**, 8139 (1990).
5) J. J. Barton and D. A. Shirley, Phys. Rev. B **32**, 1906 (1985).
6) J. J. Barton, S. W. Robey, and D. A. Shirley, Phys. Rev. B **34**, 778 (1986).
7) M.-L. Xu and M. V. Hove, Surf. Sci. **207**, 215 (1989).
8) T. Greber, J. Osterwalder, D. Naumović, A. Stuck, S. Hüfner, and L. Schlapbach, Phys. Rev. Lett. **69**, 1947 (1992).
9) Y. Chen, F. J. García de Abajo, A. Chassé, R. X. Ynzunza, A. P. Kaduwela, M. A. Van Hove, and C. S. Fadley, Phys. Rev. B **58**, 13121 (1998).
10) P. A. Martin, J. Phys. A **31**, 8923 (1998).
11) S. Omori, Y. Nihei, E. Rotenberg, J. D. Denlinger, S. Marchesini, S. D. Kevan, B. P. Tonner, M. A. Van Hove, and C. S. Fadley, Phys. Rev. Lett. **88**, 055504 (2002).
12) C. S. Fadley, M. A. V. Hove, A. Kaduwela, S. Omori, L. Zhao, and S. Marchesini, J. Phys.: Condens. Matter **13**, 10517 (2001).
13) F. Matsui, N. Nishikayama, N. Maejima, H. Matsui, K. Goto, M. Hashimoto, T. Hatayama, T. Matsushita, Y. Kato, S. Tanaka, and H. Daimon, J. Phys. Soc. Jpn. **80**, 013601 (2011).
14) A. Uesaka, K. Hayashi, T. Matsushita, and S. Arai, Phys. Rev. Lett. **107**, 045502 (2011).
15) K. Kataoka, F. Matsui, Y. Kato, F. Z. Guo, T. Matsushita, K. Hattori, and H. Daimon, Surf. Rev. Lett. **13**, 209 (2006).
16) D. P. Woodruff and A. M. Bradshaw, Rep. Prog. Phys. **57**, 1029 (1994).
17) D. Woodruff, J. Electron Spectrosc. Relat. Phenom. **126**, 55 (2002).
18) D. Woodruff, Surf. Sci. Rep. **62**, 1 (2007).
19) D. P. Woodruff, Appl. Phys. A **92**, 439 (2008).
20) C. Fadley, S. Thevuthasan, A. Kaduwela, C. Westphal, Y. Kim, R. Ynzunza, P. Len, E. Tober, F. Zhang, Z. Wang, S. Ruebush, A. Budge, and M. V. Hove, J. Electron Spectrosc. Relat. Phenom. **68**, 19 (1994).
21) C. Fadley, M. V. Hove, Z. Hussain, and A. Kaduwela, J. Electron Spectrosc. Relat. Phenom. **75**, 273 (1995).
22) C. S. Fadley, J. Electron Spectrosc. Relat. Phenom. **178–179**, 2 (2010).
23) J. Osterwalder, A. Tamai, W. Auwärter, M. P. Allan, and T. Greber,

©2018 The Author(s)

J. Phys. Soc. Jpn.
Downloaded from journals.jps.jp by 161.111.10.232 on 07/21/21

Chimia **60**, 795 (2006).
24) C. Westphal, Surf. Sci. Rep. **50**, 1 (2003).
25) E. V. Shalaeva and M. V. Kuznetsov, J. Struct. Chem. **44**, 465 (2003).
26) T. Greber, J. Phys.: Condens. Matter **13**, 10561 (2001).
27) P. Len, F. Zhang, S. Thevuthasan, A. Kaduwela, M. V. Hove, and C. Fadley, J. Electron Spectrosc. Relat. Phenom. **76**, 351 (1995).
28) M. V. Kuznetsov, I. I. Ogorodnikov, and A. S. Vorokh, Russ. Chem. Rev. **83**, 13 (2014).
29) T. Matsushita, F. Z. Guo, F. Matsui, Y. Kato, and H. Daimon, Phys. Rev. B **75**, 085419 (2007).
30) T. Matsushita, F. Matsui, H. Daimon, and K. Hayashi, J. Electron Spectrosc. Relat. Phenom. **178–179**, 195 (2010).
31) T. Matsushita, F. Matsui, K. Goto, T. Matsumoto, and H. Daimon, J. Phys. Soc. Jpn. **82**, 114005 (2013).
32) T. Matsushita and F. Matsui, J. Electron Spectrosc. Relat. Phenom. **195**, 365 (2014).
33) A. Landers, T. Weber, I. Ali, A. Cassimi, M. Hattass, O. Jagutzki, A. Nauert, T. Osipov, A. Staudte, M. H. Prior, H. Schmidt-Böcking, C. L. Cocke, and R. Dörner, Phys. Rev. Lett. **87**, 013002 (2001).
34) F. Krasniqi, B. Najjari, L. Strüder, D. Rolles, A. Voitkiv, and J. Ullrich, Phys. Rev. A **81**, 033411 (2010).
35) M. Meckel, A. Staudte, S. Patchkovskii, D. M. Villeneuve, P. B. Corkum, R. Doerner, and M. Spanner, Nat. Phys. **10**, 594 (2014).
36) K. Kobayashi, M. Kobata, and H. Iwai, J. Electron Spectrosc. Relat. Phenom. **190**, 210 (2013).
37) C. S. Fadley, Nucl. Instrum. Methods Phys. Res., Sect. A **547**, 24 (2005).
38) F. Matsui, T. Matsushita, and H. Daimon, J. Phys. Soc. Jpn. **81**, 114604 (2012).
39) F. Matsui, R. Eguchi, S. Nishiyama, M. Izumi, E. Uesugi, H. Goto, T. Matsushita, K. Sugita, H. Daimon, Y. Hamamoto, I. Hamada, Y. Morikawa, and Y. Kubozono, Sci. Rep. **6**, 36258 (2016).
40) H. Matsui, F. Matsui, N. Maejima, T. Matsushita, and H. Daimon, Surf. Sci. **635**, 1 (2015).
41) H. Matsui, F. Matsui, N. Maejima, T. Matsushita, T. Okamoto, A. N. Hattori, Y. Sano, K. Yamauchi, and H. Daimon, Surf. Sci. **632**, 98 (2015).
42) L. H. de Lima, A. de Siervo, R. Landers, G. A. Viana, A. M. B. Goncalves, R. G. Lacerda, and P. Häberle, Phys. Rev. B **87**, 081403 (2013).
43) D. Ferrah, J. Penuelas, C. Bottela, G. Grenet, and A. Ouerghi, Surf. Sci. **615**, 47 (2013).
44) D. E. Parreiras, E. A. Soares, G. J. P. Abreu, T. E. P. Bueno, W. P. Fernandes, V. E. de Carvalho, S. S. Carara, H. Chacham, and R. Paniago, Phys. Rev. B **90**, 155454 (2014).
45) F. Bianchini, L. L. Patera, M. Peressi, C. Africh, and G. Comelli, J. Phys. Chem. Lett. **5**, 467 (2014).
46) D. Y. Usachov, A. V. Fedorov, O. Y. Vilkov, A. E. Petukhov, A. G. Rybkin, A. Ernst, M. M. Otrokov, E. V. Chulkov, I. I. Ogorodnikov, M. V. Kuznetsov, L. V. Yashina, E. Y. Kataev, A. V. Erofeevskaya, V. Y. Voroshnin, V. K. Adamchuk, C. Laubschat, and D. V. Vyalikh, Nano Lett. **16**, 4535 (2016).
47) F. J. García de Abajo, M. A. Van Hove, and C. S. Fadley, Phys. Rev. B **63**, 075404 (2001).
48) L. Bignardi, P. Lacovig, M. M. Dalmiglio, F. Orlando, A. Ghafari, L. Petaccia, A. Baraldi, R. Larciprete, and S. Lizzit, 2D Mater. **4**, 025106 (2017).
49) M. Derivaz, D. Dentel, R. Stephan, M.-C. Hanf, A. Mehdaoui, P. Sonnet, and C. Pirri, Nano Lett. **15**, 2510 (2015).
50) L. H. de Lima, L. Barreto, R. Landers, and A. de Siervo, Phys. Rev. B **93**, 035448 (2016).
51) W. Auwärter, M. Muntwiler, J. Osterwalder, and T. Greber, Surf. Sci. **545**, L735 (2003).
52) M. Muntwiler, W. Auwärter, F. Baumberger, M. Hoesch, T. Greber, and J. Osterwalder, Surf. Sci. **472**, 125 (2001).
53) W. Auwärter, T. J. Kreutz, T. Greber, and J. Osterwalder, Surf. Sci. **429**, 229 (1999).
54) F. Orlando, R. Larciprete, P. Lacovig, I. Boscarato, A. Baraldi, and S. Lizzit, J. Phys. Chem. C **116**, 157 (2012).
55) R. Stania, W. Heckel, I. Kalichava, C. Bernard, T. C. Kerscher, H. Y. Cun, P. R. Willmott, B. Schönfeld, J. Osterwalder, S. Müller, and T. Greber, Phys. Rev. B **93**, 161402 (2016).
56) S. Roth, F. Matsui, T. Greber, and J. Osterwalder, Nano Lett. **13**, 2668 (2013).
57) M. Muntwiler, J. Zhang, R. Stania, F. Matsui, P. Oberta, U. Flechsig, L. Patthey, C. Quitmann, T. Glatzel, R. Widmer, E. Meyer, T. A. Jung, P. Aebi, R. Fasel, and T. Greber, J. Synchrotron Radiat. **24**, 354 (2017).
58) Y. Gamou, M. Terai, A. Nagashima, and C. Oshima, Sci. Rep. Res. Inst. Tohoku Univ. A **44**, 211 (1997).
59) K. T. Park, M. Richards-Babb, M. S. Freund, J. Weiss, and K. Klier, J. Phys. Chem. **100**, 10739 (1996).
60) D. Stoltz and S. Stoltz, Physica B **398**, 172 (2007).
61) L. Despont, F. Clerc, M. G. Garnier, H. Berger, L. Forró, and P. Aebi, Eur. Phys. J. B **52**, 421 (2006).
62) M. Kuznetsov, I. Ogorodnikov, A. Vorokh, A. Rasinkin, and A. Titov, Surf. Sci. **606**, 1760 (2012).
63) I. I. Ogorodnikov, A. S. Vorokh, A. N. Titov, and M. V. Kuznetsov, JETP Lett. **95**, 372 (2012).
64) M. Z. Hasan and C. L. Kane, Rev. Mod. Phys. **82**, 3045 (2010).
65) M. V. Kuznetsov, L. V. Yashina, J. Sánchez-Barriga, I. I. Ogorodnikov, A. S. Vorokh, A. A. Volykhov, R. J. Koch, V. S. Neudachina, M. E. Tamm, A. P. Sirotina, A. Y. Varykhalov, G. Springholz, G. Bauer, J. D. Riley, and O. Rader, Phys. Rev. B **91**, 085402 (2015).
66) D. D. dos Reis, L. Barreto, M. Bianchi, G. A. S. Ribeiro, E. A. Soares, W. S. e Silva, V. E. de Carvalho, J. Rawle, M. Hoesch, C. Nicklin, W. P. Fernandes, J. Mi, B. B. Iversen, and P. Hofmann, Phys. Rev. B **88**, 041404(R) (2013).
67) N. Fukui, T. Hirahara, T. Shirasawa, T. Takahashi, K. Kobayashi, and S. Hasegawa, Phys. Rev. B **85**, 115426 (2012).
68) M. Ye, E. Schvier, M. Nurmamat, K. Shirai, T. Matsushita, M. Morita, S. Kitagawa, R. Ishii, M. Fujita, K. Yasuda, L. Toth, H. Daimon, and T. Okuda, http://www.issp.u-tokyo.ac.jp/labs/sor/2012/user/harima/Okuda/AR2012_MaoYE.pdf.
69) J. Sánchez-Barriga, I. I. Ogorodnikov, M. V. Kuznetsov, A. A. Volykhov, F. Matsui, C. Callaert, J. Hadermann, N. I. Verbitskiy, R. J. Koch, A. Varykhalov, O. Rader, and L. V. Yashina, Phys. Chem. Chem. Phys. **19**, 30520 (2017).

Mikhail V. Kuznetsov was born in USSR in 1962. He received his Ph.D. degree in 1990 and made Habilitation in 2000. His current position is director of Institute of Solis State Chemistry of Russian Academy of Science. He is a head of the laboratory of quantum chemistry and spectroscopy. His researched interests are in the field of surface science including photoelectron diffraction and holography. He is author of 150 scientific papers.

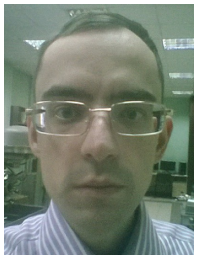

Ilya Igorevich Ogorodnikov was born in USSR in 1987. He obtained his Ph.D. in condensed matter physics in 2015 at Yekaterinburg Ural State Technical University—Ural Polytechnic Institute (USTU-UPI), Russia. He is a senior researcher at the laboratory of Institute of Solid State Chemistry of the Ural Branch of the Russian Academy of Sciences (ISSC of UB of RAS). His research activities cover the atomic structure of low-dimensional materials, including titanium dichalcogenides TiX_2 and bismuth chalcogenides Bi_2X_3 (X: S, Se, Te). The main research methods include x-ray photoelectron diffraction and photoelectron holography.

©2018 The Author(s)

J. Phys. Soc. Jpn.
Downloaded from journals.jps.jp by 161.111.10.232 on 07/21/21

Dmitry Yurievich Usachov was born in USSR in 1983. He obtained his Ph.D. in condensed matter physics in 2010 at Saint-Petersburg State University (SPbU), Russia. He was a senior researcher (until 2011) and an associate professor (2011–2017) at the department of Solid State Electronics at SPbU. Since 2017 he is a professor at SPbU. His research activities cover the electronic structure of low-dimensional materials, including graphene and h-BN on single-crystalline surfaces. The main research methods include angle- and spin-resolved photoemission, X-ray absorption and atomically-resolved scanning probe techniques.

Clemens Laubschat was born in 1955, in Berlin (Germany). He received Ph.D. degree in 1984 in experimental physics in Freie Universität Berlin; Ph.D.: "Photoemission and Bremsstrahlung-isochromat spectroscopy on heavy rare-earth compounds". He has a habilitation in 1989. He is full professor of physics, Institute for Solid-State and Materials Physics, Technische Universität Dresden (TU Dresden). His scientific interest are in solid-state physics of strongly correlated electron systems, particularly rare-earths, actinides; thin film and surface phenomena; metal–metal and metal–semiconductor interfaces, carbon-derived materials, particularly doped and intercalated graphene, bulk and surface phenomena in new materials studied by electron spectroscopy, particularly angle-resolved photoemission.

Denis Vyalikh was born in Saint-Petersburg in 1974. He obtained his Ph.D. degree in Science and Habilitation from the St. Petersburg State University in 2001 and 2012, respectively. He was worked as a beamline-scientist at Russian-German beamline (BESSY, Berlin) till 2004. Later on, he was a senior, group leader researcher in University of Technology Dresden till the end 2016. Starting from January of 2017, he acts as Ikerbasque research professor in Donosita International Physics Center in San Sebastian, Spain. His research activities cover the fine-electronic structure and exotic magnetism of rare-earth intermetallic materials as well as the properties of 2D systems based on graphene and h-BN.

Fumihiko Matsui received his Ph.D. degree in Science from the University of Tokyo in 2000. He worked as a research associate in the Graduate School of Materials Science, Nara Institute of Science and Technology (NAIST) from 2000 and currently as an associate professor. He spent one year at Universitaet Zuerich as a guest professor from 2011. He has been investigating the surface analysis techniques based on synchrotron radiation. He will move to UV-SOR in Institute of Molecular Science as a chief scientist from 2018.

Lada V. Yashina was born in 1968 in Moscow. She received her Ph.D. (1996) and D.Sc. (2008) in the field of solid-state chemistry of semiconductors and their solid-gas reactions in Lomonosov Moscow State University. He guides the group of surface science and photoelectron spectroscopy of novel materials in the Department of Inorganic Chemistry of the Lomonosov Moscow State University. Her main scientific interests include surface reactivity of carbon materials, including graphene, semiconductors, topological insulators, etc. She has published about 100 papers and contributions to books.

©2018 The Author(s)